Nano Research

Open Access

Research Article

Polarization-selective photon recycling microcavity for efficient polarized quantum-dot LEDs

Yuanjie Xia[1,2], Cuixia Yuan[1,3], Yiduo Wang[1,4], Xinyu Zhang[1,4], Heng Zhang[4] ✉, and Qiang Su[1] ✉

[1] *School of Physical Sciences, Great Bay University, Dongguan 523000, China*
[2] *School of Chemistry, University of Science and Technology of China, Hefei 230026, China*
[3] *Tsinghua Shenzhen International Graduate School, Tsinghua University, Shenzhen 518000, China*
[4] *School of Resources, Environment and Materials, Guangxi University, Nanning 530004, China*

Cite this article: *Nano Research*, **2026**, *19*, 94908755. https://doi.org/10.26599/NR.2026.94908755

ABSTRACT: The simultaneous realization of high external quantum efficiency (EQE) and high degree of polarization (DoP) in circularly polarized light-emitting diodes (LEDs) remains a substantial challenge. Here, we present a polarization-selective photon recycling microcavity integrated into a top-emitting quantum-dot LED (TE-QLED). The device incorporates a chiral Bragg-specular reflection microcavity, in which light with the opposite handedness to the Bragg layer is transmitted directly, whereas light with the same handedness undergoes chirality reversal and exits the microcavity with the opposite handedness. This polarization-selective photon recycling mechanism enables the recovery of photons that would otherwise be lost in conventional polarized light generation, thereby overcoming the physical limit of 50% loss in polarized emission. As a result, a circularly polarized QLED with a DoP of 81% (electroluminescence dissymmetry factor g_{lum}(EL) = 1.62) and a high EQE of 20.27% is achieved, with only 17.8% light loss compared to the reference device. Furthermore, a proof-of-concept three-dimensional display prototype is demonstrated, highlighting the potential of this approach for advanced display technologies.

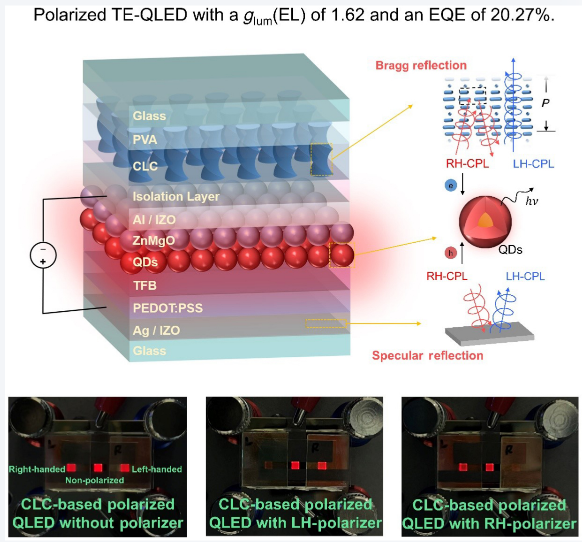

KEYWORDS: quantum-dot, light-emitting diodes, circularly polarized luminescence, cholesteric liquid crystal

1 Introduction

Quantum dots (QDs) have emerged as a promising class of luminescent material for light-emitting devices, due to their unique optical properties such as narrow emission bandwidth, tunable spectra, and compatibility with solution-processing techniques [1–11]. In recent years, fully solution-processed red, green, and blue light-emitting diodes based on QDs (QLEDs) have all achieved external quantum efficiencies (EQEs) exceeding 20% [12–22], attracting considerable interest for display and lighting applications.

Received: January 23, 2026; **Revised:** March 30, 2026
Accepted: April 20, 2026

✉Address correspondence to Heng Zhang, zhangheng@gxu.edu.cn; Qiang Su, suq@gbu.edu.cn

Building on these advances, the development of efficient circularly polarized luminescence (CPL) based on QDs has become increasingly important for a range of applications, including three-dimensional displays [23, 24], optical communications [25], and quantum technologies [26]. Conventionally, the generation of circularly polarized light is largely dependent on external polarizers, which can ensure a high degree of polarization (DoP; see definition in Note S1 in the Electronic Supplementary Material (ESM)). However, this approach inevitably results in at least 50% optical losses and increases the bulkiness of the system [27]. This fundamental photon loss is a significant disadvantage for efficient polarized light generation and motivates the development of intrinsically polarized LEDs [28, 29].

Currently, intrinsically polarized LEDs can be generally categorized into three classes according to their polarization generation mechanisms: (i) Chirality-induced polarization, commonly realized in organic light-emitting systems [30–47].

While such LEDs can achieve high EQE, their DoP remains limited (see the statistical data in Table S1 in the ESM). This constraint originates from the inherently weaker magnetic dipole transition intensity compared to electric dipole transitions in chiral organic molecules. Since the luminescence dissymmetry factor (g_{lum}) is proportional to the ratio of magnetic to electric dipole transition strengths, improving the DoP in these systems poses a fundamental challenge. (ii) Anisotropy-induced polarization, which employs anisotropic emitters such as quantum rods, nanoplatelets, and nanowires [29, 48–52]. This type of LEDs generally exhibits higher DoP, though their EQE is often compromised (Table S1 in the ESM). This is because achieving a high degree of alignment in the emissive layer typically occurs at the cost of efficient charge carrier injection [53]. (iii) Spin carrier-induced polarization, where charge carriers are polarized prior to recombination [54–65]. This type of polarized LED offers a more balanced performance between EQE and DoP, although each metric generally falls below the maximum values reported for chiral organic- or anisotropic emitter-based LEDs (see Table S1 in the ESM). The challenge lies in the efficient spin injection and spin preservation during the carrier transport process. Collectively, existing intrinsically polarized LEDs suffer from a trade-off between high efficiency and high polarization, making it challenging to achieve ideal values simultaneously.

Here, we address this challenge from a fundamentally different perspective by introducing a polarization-selective photon recycling microcavity integrated into a top-emitting QLED (TE-QLED). Notably, "polarization-selective photon recycling" here refers to a non-absorptive optical process, where rejected photons are reflected back into the cavity and converted into the desired polarization state, rather than re-absorption and re-emission [66]. A solution-processed cholesteric liquid crystal (CLC) layer is monolithically integrated into the device to provide handedness-selective Bragg reflection (Note S2 in the ESM). Notably, the emission spectrum of the QLED is matched with the Bragg reflection band of the CLC layer, enabling strong optical coupling. Together with the highly reflective bottom electrode, the CLC layer forms a Bragg-specular reflection microcavity that enables polarization-selective photon recycling for highly efficient circularly polarized emission. This microcavity not only overcomes the 50% loss limit of conventional polarized emission (see Methods for mechanism), but also does not affect the carrier injection and transport properties of the QLED. As a result, a circularly polarized TE-QLED with a DoP of 81% (corresponding to a g_{lum}(EL) of 1.62) and an EQE of 20.27% was achieved. This result confirms the simultaneous achievement of high efficiency and high polarization purity in circularly polarized QLEDs. To the best of our knowledge, this device exhibits the optimal trade-off reported to date between EQE and DoP among LEDs using external polarizers and intrinsically polarized LEDs, corresponding to a harmonic mean of 0.32. Moreover, this approach is universally applicable and can be extended to various LED systems, offering broad prospects for practical applications.

2 Results and discussion

2.1 Mechanism of the Bragg-specular reflection microcavity

Figure 1(a) illustrates the Bragg-specular reflection microcavity, which comprises an emitting layer (EML) positioned between a specular reflection interface and a Bragg reflection interface. Bragg reflection is induced via the constructive interference of light reflected from the periodic interfaces of alternating dielectric layers, which maintains the chirality of the reflected light (Note S2 in the ESM). This is achieved through the implementation of a CLC layer here. Specular reflection is the reflection of the light from a smooth surface, in which the handedness of circular polarization is inverted. In this scenario, a silver surface functions as the specular reflector.

Light emitted from the emissive layer is intrinsically unpolarized, and can be considered as a mixture of left-handed (LH) and right-handed (RH) circularly polarized components. Within the Bragg reflection band of the CLC layer, light with the same handedness as the CLC helix is selectively Bragg-reflected back into the microcavity without changing its handedness, while component with opposite handedness is transmitted directly [67–69]. Subsequently, the Bragg-reflected light undergoes specular reflection at the bottom electrode, which inverts its handedness and enables it to pass through the Bragg layer. Thanks to this design, the Bragg-specular reflection microcavity recovers photons that are typically lost in polarization modulation, enabling low-loss and highly circularly polarized output via polarization-selective photon recycling [70].

As an example, Fig. 1(b) demonstrates how LH-CPL is emitted from the Bragg-specular microcavity. The result showcases a low-loss, high-purity polarized light output, in which the microcavity selectively reverses the handedness of RH-CPL, thereby overcoming the 50% loss limit of conventional polarized emission.

Notably, the Bragg reflection of the CLC layer originates from its helical superstructure, which is realized by doping a nematic liquid crystal host with chiral dopants. The handedness and the helical pitch (defined as the distance over which the director rotates by 360°) are determined by both the concentration and the helical twisting power of the dopants [71]. This self-assembled helical architecture leads to a photonic bandgap that selectively reflects circularly polarized light within a specific wavelength range [72]. In this work, CLC mixtures composed of nematic liquid crystal E8 and chiral dopants S/R811 and S/R1011 are employed, as illustrated in Fig. 1(c). By tuning the concentration of chiral dopants, the reflection band of the CLC can be precisely matched to the QLED emission, thereby enabling efficient modulation of the output polarization, which is critical for achieving high DoP (see Note S3 in the ESM and Methods).

To evaluate the potential of the Bragg-specular reflection microcavity in inducing circularly polarized emission, it is essential to undertake a preliminary investigation into the photoluminescence (PL). As shown in Fig. 2(a), the QDs EML was excited by a 405 nm light source. The emitted light was subsequently passed through an ultraviolet (UV) filter and a polarizer before being collected by a spectrometer. Two device structures were prepared for comparison, as shown in Fig. 2(b). Sample A, consisting of a silver reflector and a red QD EML (center wavelength at 620 nm), serves as the reference. Sample B incorporates an additional CLC layer, thereby forming a Bragg-specular reflection microcavity that enables selective chirality reversal and polarized emission. Specifically, Sample B (L) employs an RH-CLC layer and thus emits LH-CPL, whereas Sample B (R) utilizes an LH-CLC layer and correspondingly emits RH-CPL. To ensure efficient polarization modulation, the reflection band of the CLC layer was adjusted to overlap with the emission spectrum of the red QDs, as shown in Fig. 2(c). This was achieved by altering the concentration of chiral dopants in the nematic host E8, thereby tuning the helical pitch of the CLC. Specifically, a ternary mixture

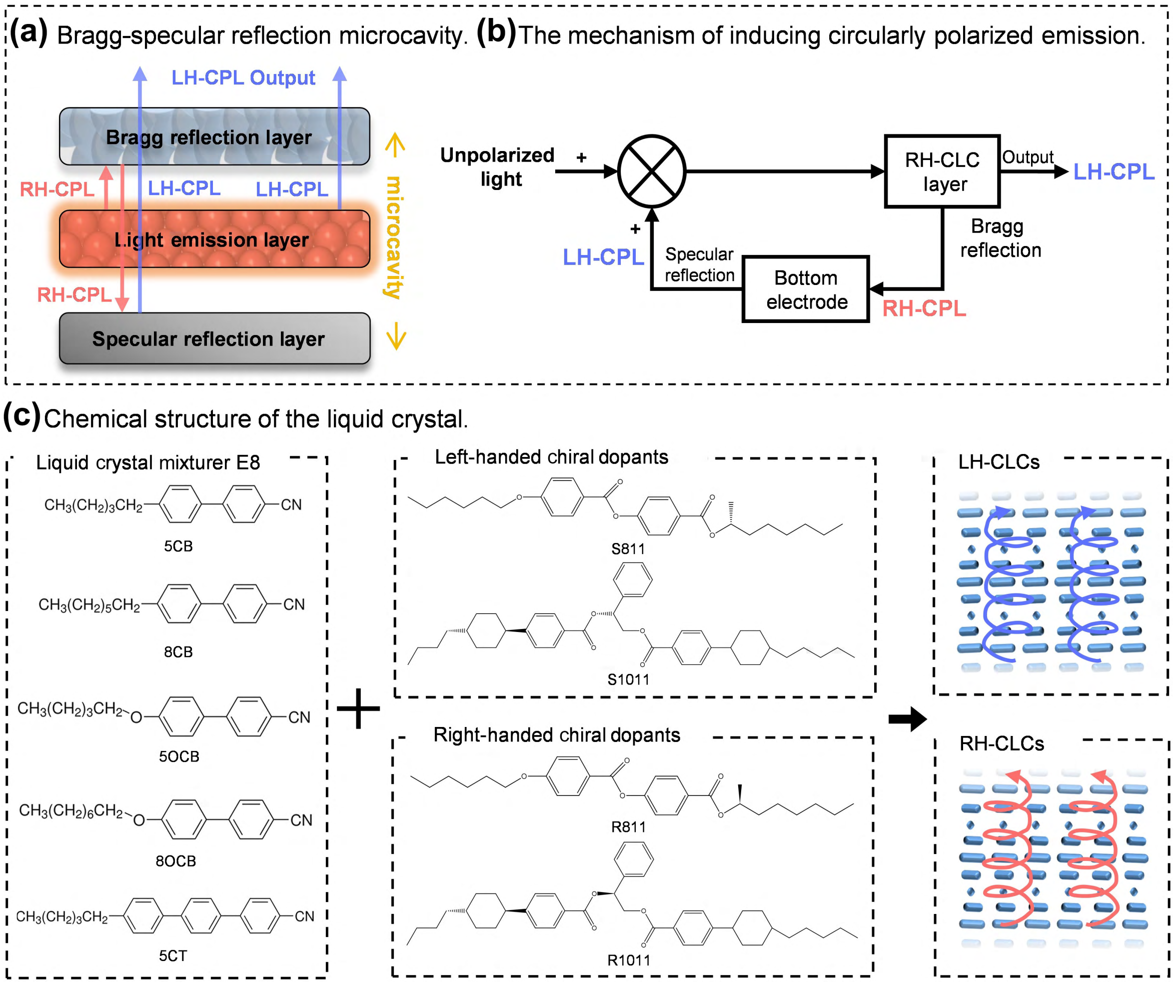

Figure 1 Design and working principle of the Bragg-specular reflection microcavity. (a) Schematic structure of a Bragg-specular reflection microcavity. (b) Mechanism of the Bragg-specular microcavity induced circularly polarized emission. (c) Chemical structures of the nematic liquid crystal host (E8) and chiral dopants (S/R811 and S/R1011), which self-assemble into CLC helical superstructure.

of S/R811, S/R1011, and E8 in a weight ratio of 10:4:86 was prepared, whose reflection band precisely covers the QD emission range, enabling strong coupling between the EML and the Bragg-specular reflection microcavity. As shown in Fig. 2(d), sample B (L) exhibit LH-CPL emission intensities corresponding to 89.5% of the total emission of sample A at normal direction. In addition, a residual 5.1% of RH-emission remains in sample B (L). Since the PL of QDs is intrinsically unpolarized, these results indicate that approximately 39.5% of the RH-CPL component is converted into LH-CPL through chirality reversal in the Bragg-specular reflection microcavity of sample B (L) at normal direction. The PL intensity of LH-CPL and RH-CPL components of sample B (L) is provided in Fig. S7 in the ESM. In Fig. 2(e), the angular emission profile of sample A and B (L) is measured. According to the result, the angular emission profile of sample A is nearly Lambertian. In contrast to sample A, sample B exhibits enhanced forward directivity for the left-handed circularly polarized component. Meanwhile, the right-handed component is significantly suppressed in the forward direction. In addition, time-resolved photoluminescence (TRPL) measurements in Fig. S8 in the ESM show identical radiative decay rates of sample A and B, indicating that the Purcell effect is negligible in sample B. Therefore, the observed angular emission profile can be attributed to polarization-selective photon recycling mechanism, further supporting that a portion of the circularly polarized light undergoes chirality reversal within the cavity.

Subsequently, the variation of DoP with observation angle is summarized in Fig. 2(f), indicating that the PL samples exhibit distinct angular behaviors. This originates from the angle-dependent blue shift of the Bragg reflection band, which reduces the overlap with the emission spectrum and thus lowers the DoP at large viewing angles. The maximum dissymmetry factor of PL [g_{lum}(PL)] reaches 1.83 at normal incidence and decreases sharply beyond ±40°. These results confirm that the Bragg-specular reflection microcavity enables effective chirality reversal and handedness modulation by selectively converting one helicity into the other.

2.2 Circularly polarized QLED

In addition to the chirality reversal property of the Bragg-specular reflection microcavity, another significant advantage of this design is its capacity to facilitate monolithic integration with QLEDs without compromising their electrical performance. As demonstrated in Fig. 3(a), this integration was achieved using a TE-QLED structure (see Note S4 in the ESM), wherein a CLC layer was directly fabricated above the QLED (see Methods). In this configuration, a highly transparent IZO (100 nm) cathode ensures

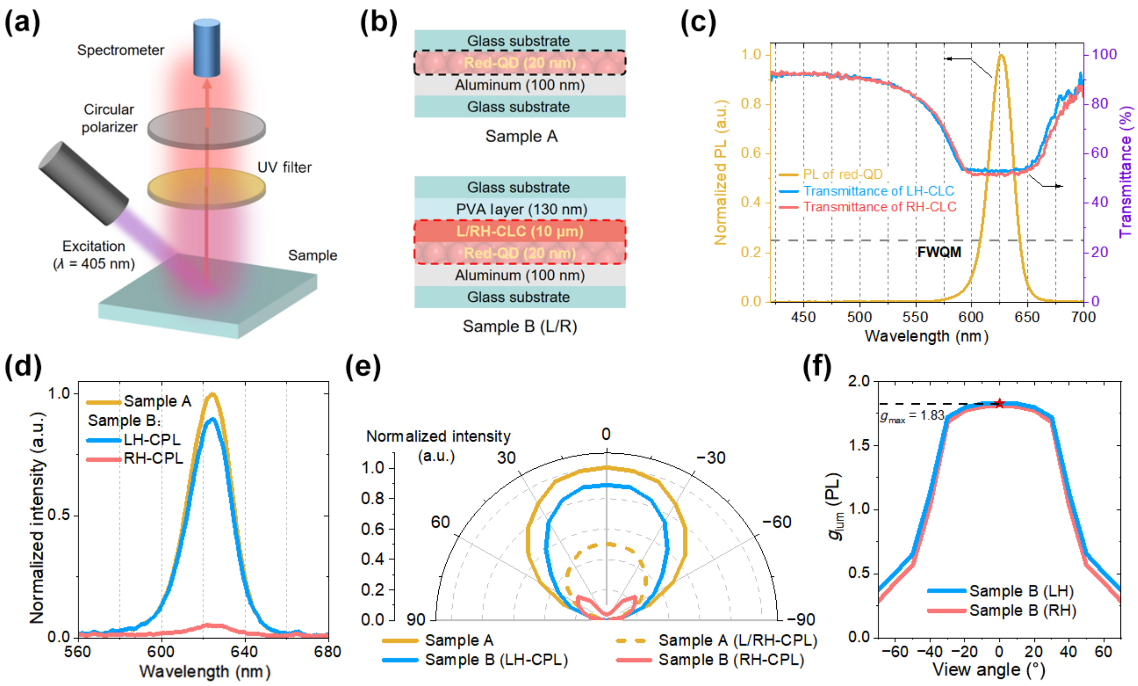

Figure 2 PL characterization of Bragg-specular reflection microcavities. (a) Experimental setup for PL measurements. (b) Reference sample A (without a cavity) and sample B (L/R) with a Bragg-specular reflection microcavity composed of LH/RH CLCs, which emits RH- and LH-CPL, respectively. (c) Emission spectrum of red QDs and transmittance of LH/RH CLC cells. (d) PL spectra of sample A and sample B (L) under photoexcitation, where sample B is further divided into LH-CPL and RH-CPL components. (e) Angular emission profiles of PL sample A and B. (f) Dissymmetry factor g_{lum}(PL) at different emission angles.

efficient electron injection and output of light, while the bottom Ag/IZO (100 nm/10 nm) anode serves as a specular reflector. Together, the CLC-based Bragg reflector and the metallic anode form a Bragg-specular microcavity that yields polarized emission. This architecture exhibits broad compatibility and can be monolithically integrated into a wide range of LED systems. The electro-optical performance of the polarized QLEDs was then evaluated using the characterization setup shown in Fig. 3(b). The source meter provides step driving voltages to the device, while the photodetector collects emitted photons. The photon counts are then converted to optical power using the measured EL spectra, from which the EQE and *J*–*V*–*L* characteristics are derived. Notably, the polarizer is applied for measuring the angular emission profile, whereas EQEs are measured without it. The CLC layer is highly sensitive to temperature, and QLEDs generate substantial heat during prolonged operation at high brightness. Therefore, we first evaluated the thermal stability of the polarized-QLED. Our results show that when the device operates at a brightness ranging from 5000 to 100,000 cd/m^2, the temperature remains below 35 °C (Figs. 3(c) and 3(d)), which is well within the range that preserves the optical performance of the CLC layer. Figure 3(c) presents infrared imaging of the QLED during operation, revealing a temperature increase from 21.3 °C at 2 V (210 cd/m^2) to 33.8 °C at 6 V (75670 cd/m^2). Figure 3(d) displays the temperature-dependent transmittance of the CLC layer and the corresponding operating temperature from 21.3 to 33.8 °C of the QLED under different applied voltages, revealing that the optical properties of CLC layer maintain stability within this temperature range.

The Bragg-specular microcavity exhibits outstanding polarization output characteristics, enabling the EL intensity of the LH-CPL to be regulated to 88.38% of the total emission (see Fig. 3(e)). It is noted that a minor proportion of photons are emitted as RH-CPL, which can be attributed to factors such as defects in the CLC layer or large emission angles. Subsequently, the CLC layer with micrometer-scale thickness was monolithically integrated into the QLED, without adversely affecting the carrier injection and transport. The EL intensity of the RH-polarized QLED, along with its LH-CPL and RH-CPL components, is provided in Fig. S9 in the ESM. As shown in Fig. 3(f), the turn-on voltage and current density remain essentially unchanged. The luminance of the polarized QLED reaches approximately 82.2% of that of the reference device, indicating that the integration of the Bragg-specular reflection microcavity results in only a slight light loss of 17.8%, which is far below the fundamental 50% loss imposed by an ideal external polarizer. Ultimately, the EQE comparison in Fig. 3(g) shows that the polarized-QLED maintains a high EQE of 20.27%, while the maximum EQE of the reference device is 24.66%.

Moreover, the g_{lum}(EL) can be calculated from the EL spectra, as shown in Fig. 4(a). The LH and RH polarized QLED exhibit the maximum EL of 1.62 and −1.61, corresponding to DoP of 81% and 80.5%, respectively. The angular emission characteristics are presented in Fig. 4(b), taking the LH polarized QLED as an example. At normal observation (perpendicular to the device surface), the RH-CPL component is strongly suppressed, yielding the maximum EL of 1.62. As the viewing angle increases, the suppression of the opposite helicity weakens. Eventually, the emission becomes nearly unpolarized at an angle of 40°. Notably, the PL samples exhibit a near-Lambertian emission profile because the external excitation uniformly excites the emitters and their dipoles are randomly oriented, leading to isotropic emission. In contrast, the EL samples exhibit a significant angular dependence due to microcavity effects originating from the functional layers. Consequently, the angular emission profiles of the PL and EL samples are slightly different, with the PL sample exhibiting a high DoP over a wider range of observation angles. The variation of DoP with observation angle is summarized in Fig. 4(c), illustrating the

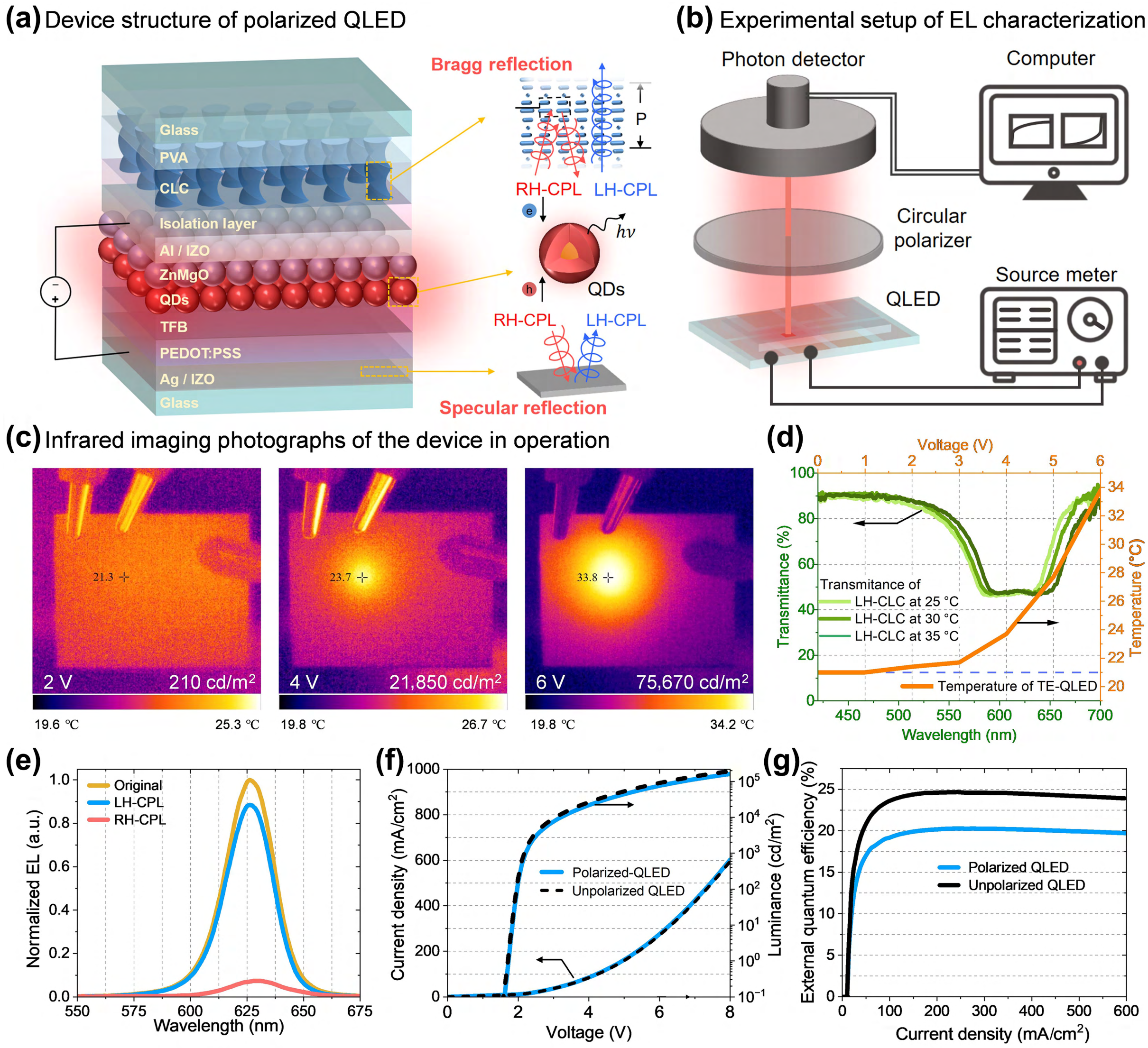

Figure 3 The thermal and electro-optical performance of polarized QLEDs. (a) Device structure of the Bragg-specular reflection microcavity-based polarized QLED. (b) Schematic of the experimental setup used for EL characterization. (c) Infrared imaging photographs of the QLED in operation. (d) Temperature-dependent transmittance of the CLC layer and the corresponding operating temperature of the QLED under different applied voltages. (e) EL spectra of the LH-polarized QLED, showing total emission and the decomposed LH-CPL and RH-CPL components. (f) *J*–*V*–*L* characteristics of the polarized QLED compared with the unpolarized reference QLED. (g) EQE comparison between the polarized QLED and the reference QLED.

angular dependence of polarization retention in the Bragg-specular reflection microcavity. Finally, Fig. 4(d) compares our results with previous publications on polarized LEDs based on different polarization mechanisms, including chirality-induced, anisotropy-induced, and spin carriers-induced polarization. Earlier approaches have generally been unable to achieve both high DoP and high EQE simultaneously. In contrast, the Bragg-specular reflection microcavity offers an innovative solution that achieves a DoP of 81% and an EQE of 20.27%, representing a promising balance between DoP and EQE. To further quantify the balance between the EQE and the DoP, we introduce the Harmonic mean (*H*) as a quantitative metric. It is defined by the formula

$$H = \frac{(2 \times \text{EQE} \times \text{DoP})}{(\text{EQE} + \text{DoP})} \tag{1}$$

The Harmonic mean exhibits a high sensitivity to lower values; consequently, it yields a high value only when both EQE and DoP are high and decreases significantly if either value is low. As shown in Fig. 4(d), our polarized QLED achieves a Harmonic mean of 0.32. Notably, the theoretical maximum *H* is 0.4 (when EQE = 25% and DoP = 1). This high value demonstrates the successful co-realization of high-efficiency and high-purity circularly polarized EL.

2.3 Three-dimensional display based on circularly polarized QLEDs

To provide a visualized demonstration, three QLEDs with different polarization statuses (LH, unpolarized, and RH) were integrated sequentially from left to right on a single glass substrate. This configuration enables direct visual comparison of their polarization properties under identical conditions. As shown in Fig. 5(a), without any polarization filter, the three devices exhibit similar brightness. When a LH circular polarizer is applied (Fig. 5(b)), the LH device appears darker, while the unpolarized and RH devices

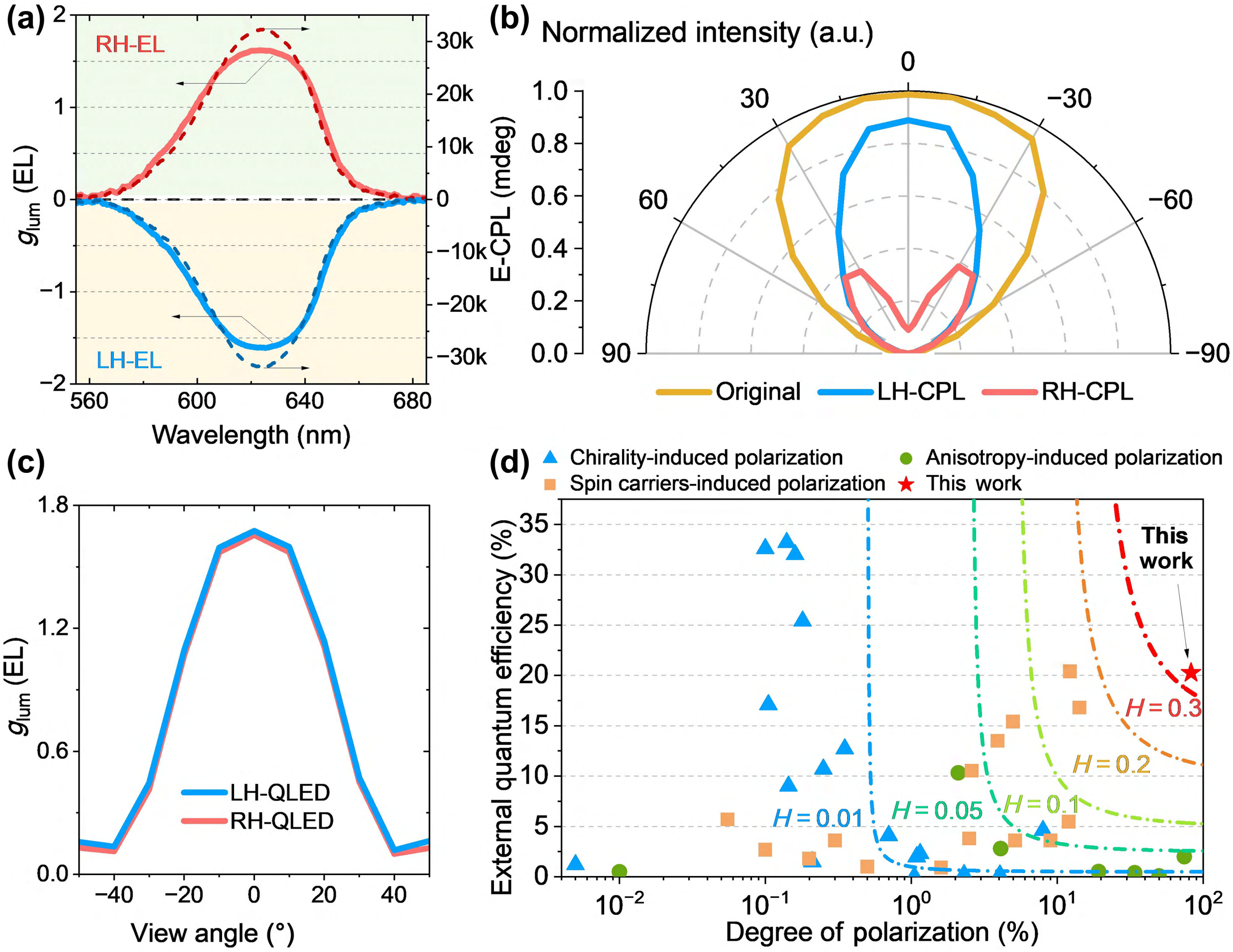

Figure 4 Electroluminescence dissymmetry characteristics of polarized QLEDs. (a) Calculated EL dissymmetry factor (g_{lum}(EL)) and E-CPL values. (b) Angular emission profiles of the P-QLED, including total, LH-CPL, and RH-CPL components. (c) Dissymmetry factor g_{lum}(EL) at different emission angles. (d) Comparison of DoP and EQE with previous work with Harmonic mean (*H*).

remain bright. In contrast, with a RH circular polarizer (Fig. 5(c)), the LH and unpolarized devices appear bright, whereas the RH device is strongly suppressed. These results provide a clear and straightforward verification of the circular polarization characteristics of the devices. To further verify the potential of circularly polarized QLEDs for three-dimensional (3D) display applications, a proof-of-concept 3D visualization prototype was demonstrated, as illustrated in Figs. 5(d)–5(h). A QLED device was patterned with a shape of flower encoded into LH and RH polarization channels, which can be selectively observed through corresponding circular polarizers in 3D glasses. Figures 5(e) and 5(f) show the images observed by the left and right eyes (also watch Video S1 in the ESM), respectively: under a LH polarizer, only the right-side flower is visible, whereas under a RH polarizer, the left-side flower is visible. The working principle is illustrated in Figs. 5(g) and 5(h). When the left eye observes the right-side image and the right eye observes the left-side image, the human brain fuses the two views into a virtual image projected in front of the screen (Fig. 5(g)). In contrast, when the left eye views the left-side image and the right eye views the right-side image, the virtual image is perceived behind the screen(Fig. 5(h)). These results demonstrate the potential of Bragg-specular microcavity-induced QLEDs to realize 3D displays.

3 Conclusion

We demonstrate a circularly polarized QLED that simultaneously achieves high polarization and high efficiency via polarization-selective photon recycling enabled by a Bragg-specular reflection microcavity. This device design effectively mitigates the inherent photon loss in the polarization modulation while preserving the intrinsic electrical characteristics of the QLED. Consequently, a polarized QLED with a DoP of 81% and an EQE of 20.27% is realized, exhibiting only an 17.8% photon loss compared to an unpolarized QLED with an identical structure. These results demonstrate a circular polarization conversion efficiency exceeding 50% enabled by the Bragg-specular reflection microcavity, thereby overcoming the fundamental physical limit imposed by conventional polarization filtering. Additionally, the harmonic mean of the EQE and DoP reaches 0.32, which, to the best of our knowledge, is the highest value reported to date for intrinsically polarized LEDs and underscores an excellent balance between efficiency and polarization performance. Notably, the polarization-selective photon recycling microcavity is applicable to various LED systems. Furthermore, we highlight the potential of the developed polarized QLED for applications in 3D display technologies. Overall, this work demonstrates that a polarization-selective photon recycling mechanism enabled by a Bragg-specular reflection

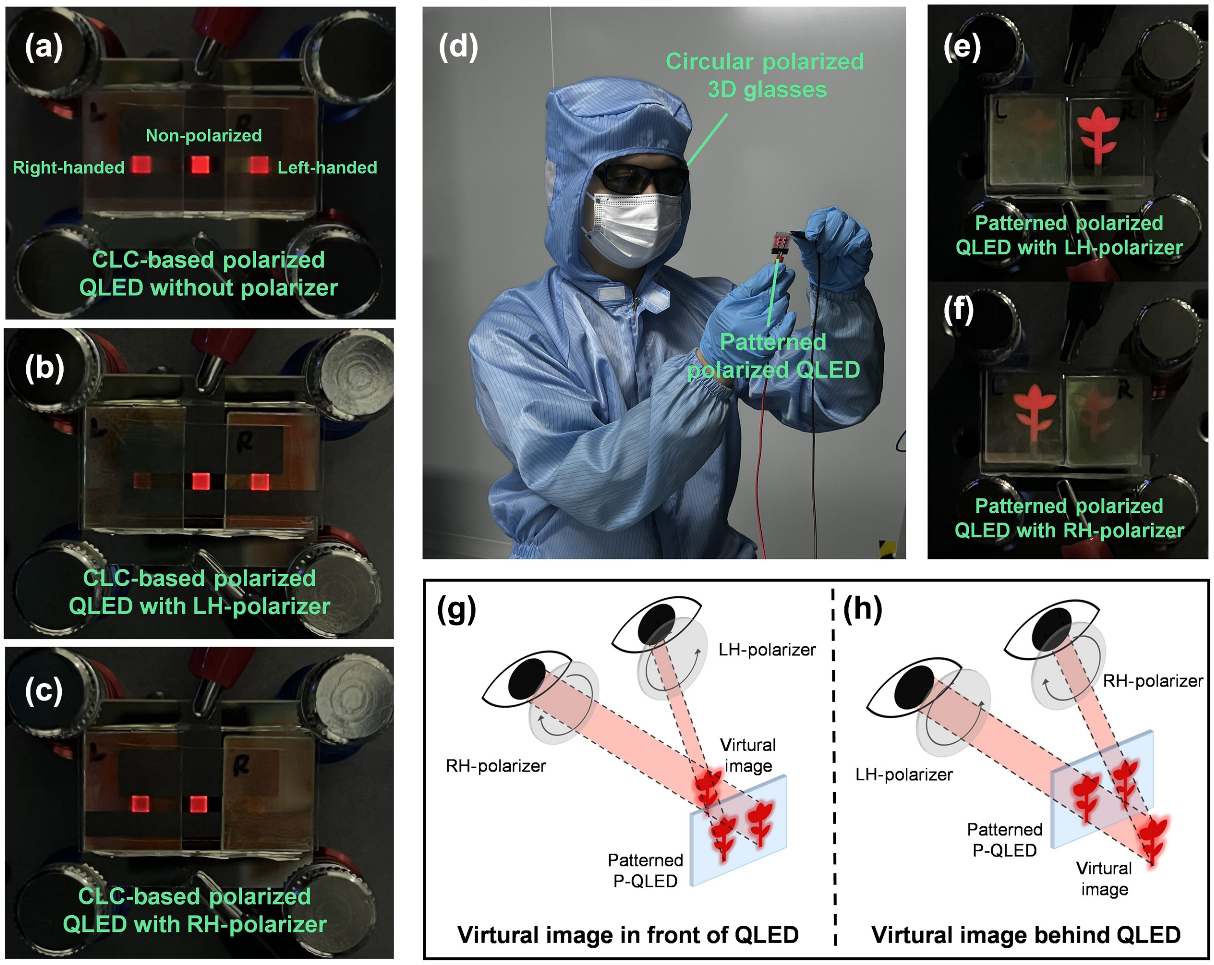

Figure 5 Demonstration of 3D display using circularly polarized QLEDs. (a)–(c) Photographs of three QLED pixels (left-handed, unpolarized, right-handed) integrated on a single glass substrate under different observation conditions: (a) without a polarizer, (b) with an LH-polarizer, and (c) with an RH-polarizer. (d) Observation of patterned polarized QLED using 3D glasses. (e) and (f) Images observed by the left and right eyes, respectively, when viewing a QLED with a flower pattern. (g) and (h) Working principle of stereoscopic imaging: (g) the left eye viewing the right image while the right eye viewing the left image (virtual image in front of the device), and (h) the left eye viewing the left image while the right eye viewing the right image (virtual image behind the device).

microcavity can surpass the conventional 50% polarization loss limit, offering a promising solution toward highly efficient circularly polarized light sources.

4 Methods

4.1 Materials

All materials were commercially available. CdSe QDs suspension (λc at 620 nm, 25 mg/mL in octane) was purchased from Suzhou Xingshuo Nanotech Co., Ltd. ZnMgO suspension (50 mg/mL in Ethanol) was purchased from Guangdong Poly Optoelectronics Co., Ltd. Poly[(9,9-dioctylfluorenyl-2,7-diyl)-co-(4,4'-(N-(pbutylphenyl))diphenylamine)] (TFB) was purchased from VOLT-AMP Optoelectronic Technology Co., Ltd. PEDOT:PSS 4083 (poly(3,4-ethylenedioxythiophene)-poly(styrenesulfonate), 1.3 wt.%–1.7 wt.% in water) was purchased from Luminescence Technology Corp. IZO, Ag target materials were purchased from Zhongnuoxincai Co., Ltd. Ethanol, chlorobenzene, and octane were purchased from Aladdin Industrial Corp. Liquid crystal mixture E8, chiral dopants S/R 811, and S/R 1011 were purchased from Nanjing Xinyao Technology Co., Ltd. The UV-curable adhesives NOA63 and NOA89 were purchased from Norland Products, Inc. CdSe QDs suspension was diluted to a concentration of 15 mg/mL in octane. ZnMgO suspension was diluted to a concentration of 25 mg/mL in ethanol. TFB was dissolved in chlorobenzene at a concentration of 6 mg/mL. L-CLC was prepared by doping S811 and S1011 into the nematic host E8 at a weight ratio of 10:4:86, followed by stirring at 80 °C until fully homogenized. Similarly, R-CLC was prepared by replacing the chiral dopants with R811, R1011 in the same procedure.

4.2 Device structure

For the PL experiment, sample A comprised Glass/Ag (100 nm)/red QDs (20 nm)/Glass, containing only the silver specular reflector and QD emitting layer (λc at 620 nm). The structure of sample B is Glass/Ag (100 nm)/red QDs (20 nm)/CLC (10 μm)/PVA (130 nm)/Glass. In sample B, the PVA layer served as an alignment layer to ensure a uniform orientation of the CLC material at the surface. The thickness of the CLC layer can be controlled by adjusting the injected volume of the CLC material according to the area of the top substrate. In this work, the CLC layer thickness was chosen to be 10 μm, ensuring complete Bragg reflection within the designed spectral range. Further details are provided in the ESM.

For the EL experiment, the polarized QLED was fabricated with

Glass/Ag (100 nm)/IZO (10 nm)/PEDOT:PSS (35 nm)/TFB (25 nm)/QDs (20 nm)/ZnMgO (55 nm)/Al (2 nm)/IZO (100 nm)/NOA 89 (3 μm)/CLC (10 μm)/PVA (130 nm)/Glass. The reference TE-QLED was fabricated with Glass/Ag (100 nm)/IZO (10 nm)/PEDOT:PSS (35 nm)/TFB (25 nm)/QDs (20 nm)/ZnMgO (55 nm)/Al (2 nm)/IZO (100 nm).

4.3 Device fabrication

For the PL experiment, sample A was fabricated using the following procedure. Initially, a glass substrate was first coated with 100 nm of Ag via sputter deposition. Subsequently, the red CdSe QD suspension (15 mg/mL in octane) was spin-coated on the Ag layer at 3000 rpm for 45 s and then baked at 100 °C for 5 min to evaporate the solvent. The surface morphology of the QD layer was characterized by atomic force microscopy (AFM), as shown in Fig. S10 in the ESM. The sample was then sealed with a cover glass by UV-curable adhesive NOA 63. Sample B included an extra CLC layer and a PVA layer. Sample B followed the same procedure as sample A, but included an additional CLC and PVA layer. PVA (5 wt.% in water) was spin-coated on a clean cover glass at 3000 rpm to achieve a 130 nm film, baked at 100 °C for 10 min, and unidirectionally rubbed with a nylon cloth to form the alignment layer. Afterwards, 2 μL of the CLC material was dispensed onto an unsealed sample A and uniformly spread using a 2 cm^2 PVA-coated cover glass.

For the EL experiment, the reference TE-QLEDs were fabricated following a sequential layer deposition process. First, the bottom electrodes were prepared by sputter-coating a silver layer followed by an IZO layer onto glass substrates. PEDOT:PSS layer (4083) was then spin-coated at 3000 rpm for 45 s and baked at 130 °C for 20 min. Subsequently, a TFB layer was spin-coated at 2000 rpm for 45 s and baked at 120 °C for 20 min. The QD layer was spin-coated at 3000 rpm for 45 s and baked at 100 °C for 5 min. A ZnMgO layer was then spin-coated at 3000 rpm and baked at 100 °C for 10 min. To improve electron injection and device performance, an aluminum layer with a thickness of 2 nm was evaporated, followed by sputter deposition of a 100 nm-thick IZO top electrode as the cathode. Polarized QLEDs were fabricated following the same procedure as the TE-QLEDs described above, with an additional isolation layer, CLC layer, and PVA alignment layer. UV-curable adhesive NOA 89 was used as an isolation layer to prevent CLC-induced damage to the existing device structure (see Note S5 in the ESM). Based on the TE-QLED structure, NOA 89 was spin-coated onto the IZO cathode at 3000 rpm for 45 s and cured under UV light for 2 min, with a thickness of 3 μm. Subsequently, 4 μL of the CLC material was dropped onto the adhesive layer and spread evenly using a 4 cm^2 PVA-coated cover glass.

4.4 Characterization

The thicknesses of the functional layers were measured through a KLA Tencor P-7 Stylus Profiler. Differential scanning calorimetry (DSC, DSC 300 Caliris Select, NETZSCH) was used to measure the phase transition temperatures of the CLC material. The surface morphology of the QD layer was characterized using an AFM (Dimension Icon, Bruker). The spectrum of PL and EL at different wavelengths was measured with an Ocean Optics spectrometer (USB2000). The transmittance of CLC cells was also measured by USB2000 using transmittance mode. J–V–L, EQE properties were characterized by a dual-channel programmable source meter (Keithley 2612B) with a PIN-25D–calibrated silicon photodiode. The emission solid angle of the QLED was measured by the Xipu Optoelectronics Angle Resolution Test System.

Electronic Supplementary Material: Supplementary material ((1) definition and calculations for EQE and DoP; (2) Bragg reflection in cholesteric liquid crystals; (3) preparation of cholesteric liquid crystal mixture; (4) device structure and operation mechanism of the TE-QLED; (5) selection and processing of the isolation layer; (6) spectrum of exciting light and absorption of red QDs; (7) PL spectra of RH-polarized QLED; (8) TrPL of samples A and B; (9) EL spectra of RH-polarized QLED; (10) AFM image of QD layer; (11) summary of previous studies on polarized LEDs) is available in the online version of this article at https://doi.org/10.26599/NR.2026.94908755.

Data availability

All data needed to support the conclusions in the paper are presented in the manuscript and the Electronic Supplementary Material. Additional data related to this paper may be requested from the corresponding author upon request.

Acknowledgements

This work was supported by the National Natural Science Foundation of China (No. 62404027) and Natural Science Foundation of Guangdong Province (No. 2025A1515012186).

Declaration of competing interest

The authors declare no competing financial interests.

Author contribution statement

Q. S. and Y. J. X. conceived the idea. Q. S. supervised the work and provided critical revisions to the final manuscript. Y. J. X. conducted the experiments, collected the data, drew the figures and wrote the first draft of the manuscript. H. Z. contributed to scientific discussion and manuscript revision. C. X. Y., Y. D. W. and X. Y. Z. discussed the results and reviewed the manuscript.

Use of AI statement

None.

References

[1] Dai, X. L.; Zhang, Z. X.; Jin, Y. Z.; Niu, Y.; Cao, H. J.; Liang, X. Y.; Chen, L. W.; Wang, J. P.; Peng, X. G. Solution-processed, high-performance light-emitting diodes based on quantum dots. *Nature* **2014**, *515*, 96–99.

[2] Won, Y. H.; Cho, O.; Kim, T.; Chung, D. Y.; Kim, T.; Chung, H.; Jang, H.; Lee, J.; Kim, D.; Jang, E. Highly efficient and stable InP/ZnSe/ZnS quantum dot light-emitting diodes. *Nature* **2019**, *575*, 634–638.

[3] Kim, T.; Kim, K. H.; Kim, S.; Choi, S. M.; Jang, H.; Seo, H. K.; Lee, H.; Chung, D. Y.; Jang, E. Efficient and stable blue quantum dot light-emitting diode. *Nature* **2020**, *586*, 385–389.

[4] Bian, Y. Y.; Yan, X. H.; Chen, F.; Li, Q.; Li, B.; Hou, W. J.; Lu, Z. Z.; Wang, S. B.; Zhang, H.; Zhang, W. J. et al. Efficient green InP-based QD-LED by controlling electron injection and leakage. *Nature* **2024**, *635*, 854–859.

[5] Wu, Q. Q.; Cao, F.; Yu, W. K.; Wang, S.; Hou, W. J.; Lu, Z. Z.; Cao,

W. R.; Zhang, J. Q.; Zhang, X. Y.; Yang, Y. G. et al. Homogeneous ZnSeTeS quantum dots for efficient and stable pure-blue LEDs. *Nature* **2025**, *639*, 633–638.

[6] Meng, T. T.; Zheng, Y. T.; Zhao, D. L.; Hu, H. L.; Zhu, Y. B.; Xu, Z. W.; Ju, S. M.; Jing, J. P.; Chen, X.; Gao, H. J. et al. Ultrahigh-resolution quantum-dot light-emitting diodes. *Nat. Photonics* **2022**, *16*, 297–303.

[7] Yoo, J.; Lee, K.; Yang, U. J.; Song, H. H.; Jang, J. H.; Lee, G. H.; Bootharaju, M. S.; Kim, J. H.; Kim, K.; Park, S. I. et al. Highly efficient printed quantum dot light-emitting diodes through ultrahigh-definition double-layer transfer printing. *Nat. Photonics* **2024**, *18*, 1105–1112.

[8] Kim, D. C.; Seung, H.; Yoo, J.; Kim, J.; Song, H. H.; Kim, J. S.; Kim, Y.; Lee, K.; Choi, C.; Jung, D. et al. Intrinsically stretchable quantum dot light-emitting diodes. *Nat. Electron.* **2024**, *7*, 365–374.

[9] Xu, H. Y.; Song, J. J.; Zhou, P. H.; Song, Y.; Xu, J.; Shen, H. B.; Fang, S. C.; Gao, Y.; Zuo, Z. J.; Pina, J. M. et al. Dipole-dipole-interaction-assisted self-assembly of quantum dots for highly efficient light-emitting diodes. *Nat. Photonics* **2024**, *18*, 186–191.

[10] Su, Q.; Chen, Z. N.; Chen, S. M. Tracing the electron transport behavior in quantum-dot light-emitting diodes via single photon counting technique. *Nat. Commun.* **2024**, *15*, 8150.

[11] Zhou, T. H.; Tian, F. S.; Chen, S. M. Nanosecond-pulsed electroluminescence from high current-driven quantum-dot light-emitting diodes. *Sci. Adv.* **2025**, *11*, eads1388.

[12] Shen, H. B.; Gao, Q.; Zhang, Y. B.; Lin, Y.; Lin, Q. L.; Li, Z. H.; Chen, L.; Zeng, Z. P.; Li, X. G.; Jia, Y. et al. Visible quantum dot light-emitting diodes with simultaneous high brightness and efficiency. *Nat. Photonics* **2019**, *13*, 192–197.

[13] Moon, H.; Lee, C.; Lee, W.; Kim, J.; Chae, H. Stability of quantum dots, quantum dot films, and quantum dot light-emitting diodes for display applications. *Adv. Mater.* **2019**, *31*, 1804294.

[14] Pu, C. D.; Dai, X. L.; Shu, Y. F.; Zhu, M. Y.; Deng, Y. Z.; Jin, Y. Z.; Peng, X. G. Electrochemically-stable ligands bridge the photoluminescence-electroluminescence gap of quantum dots. *Nat. Commun.* **2020**, *11*, 937.

[15] Lee, T.; Kim, B. J.; Lee, H.; Hahm, D.; Bae, W. K.; Lim, J.; Kwak, J. Bright and stable quantum dot light-emitting diodes. *Adv. Mater.* **2022**, *34*, 2106276.

[16] Deng, Y. Z.; Peng, F.; Lu, Y.; Zhu, X. T.; Jin, W. X.; Qiu, J.; Dong, J. W.; Hao, Y. L.; Di, D. W.; Gao, Y. et al. Solution-processed green and blue quantum-dot light-emitting diodes with eliminated charge leakage. *Nat. Photonics* **2022**, *16*, 505–511.

[17] Chen, X. T.; Lin, X. F.; Zhou, L. K.; Sun, X. J.; Li, R.; Chen, M. Y.; Yang, Y. X.; Hou, W. J.; Wu, L. J.; Cao, W. R. et al. Blue light-emitting diodes based on colloidal quantum dots with reduced surface-bulk coupling. *Nat. Commun.* **2023**, *14*, 284.

[18] Gao, Y.; Li, B.; Liu, X. N.; Shen, H. B.; Song, Y.; Song, J. J.; Yan, Z. J.; Yan, X. H.; Chong, Y. H.; Yao, R. Y. et al. Minimizing heat generation in quantum dot light-emitting diodes by increasing quasi-Fermi-level splitting. *Nat. Nanotechnol.* **2023**, *18*, 1168–1174.

[19] Jang, E.; Jang, H. Review: Quantum dot light-emitting diodes. *Chem. Rev.* **2023**, *123*, 4663–4692.

[20] Li, M. Q.; Li, R.; Wu, L. J.; Lin, X. F.; Xia, X. Q.; Ao, Z. T.; Sun, X. J.; Chen, X. T.; Chen, S. Ultrabright and stable top-emitting quantum-dot light-emitting diodes with negligible angular color shift. *Nat. Commun.* **2024**, *15*, 5161.

[21] Chen, Z. N.; Yuan, C. X.; Chen, S. M. Micrometer-scale-thick quantum-dot LEDs with notably enhanced stability and ultrahigh brightness. *Sci. Adv.* **2025**, *11*, eads7770.

[22] Li, H. T.; Wang, J. M.; Chen, S. M. Face-to-face integrated tandem quantum-dot LEDs with high performance and multifunctionality. *Light: Sci. Appl.* **2025**, *14*, 171.

[23] Guo, Y. C.; Zhang, Y. F.; Ma, J. F.; Liao, R.; Wang, F. Wide-range tunable circularly polarized luminescence in triphenylamine supramolecular polymers via charge-transfer complexation. *Nat. Commun.* **2024**, *15*, 9303.

[24] Zhang, M. J.; Guo, Q.; Li, Z. Y.; Zhou, Y. J.; Zhao, S. S.; Tong, Z.; Wang, Y. X.; Li, G. G.; Jin, S.; Zhu, M. Z. et al. Processable circularly polarized luminescence material enables flexible stereoscopic 3D imaging. *Sci. Adv.* **2023**, *9*, eadi9944.

[25] Liu, Q.; Wei, Q.; Ren, H.; Zhou, L. W.; Zhou, Y. F.; Wang, P. Z.; Wang, C. H.; Yin, J.; Li, M. J. Circular polarization-resolved ultraviolet photonic artificial synapse based on chiral perovskite. *Nat. Commun.* **2023**, *14*, 7179.

[26] Wan, L.; Liu, Y. Z.; Fuchter, M. J.; Yan, B. H. Anomalous circularly polarized light emission in organic light-emitting diodes caused by orbital-momentum locking. *Nat. Photonics* **2023**, *17*, 193–199.

[27] Land, E. H. Some aspects of the development of sheet polarizers. *J. Opt. Soc. Am.* **1951**, *41*, 957–963.

[28] Wang, M.; Yang, Z. W.; Zhang, C. Polarized photoluminescence from lead halide perovskites. *Adv. Opt. Mater.* **2021**, *9*, 2002236.

[29] Ye, J. Z.; Ren, A. B.; Dai, L. J.; Baikie, T. K.; Guo, R. J.; Pal, D.; Gorgon, S.; Heger, J. E.; Huang, J. Y.; Sun, Y. Q. et al. Direct linearly polarized electroluminescence from perovskite nanoplatelet superlattices. *Nat. Photonics* **2024**, *18*, 586–594.

[30] Hong, J.; Kim, S.; Park, G.; Lee, Y.; Kim, H.; Kim, S.; Lee, T. W.; Kim, C.; You, Y. N. M. Chiral polymer hosts for circularly polarized electroluminescence devices. *Chem. Sci.* **2021**, *12*, 8668–8681.

[31] Moreno-Naranjo, J. M.; Furlan, F.; Wang, J. X.; Ryan, S. T. J.; Matulaitis, T.; Xu, Z. Y.; Zhang, Q. Y.; Minion, L.; Di Girolamo, M.; Jávorfi, T. et al. Enhancing circularly polarized electroluminescence through energy transfer within a chiral polymer host. *Adv. Mater.* **2024**, *36*, 2402194.

[32] Xu, L. T.; Liu, H.; Peng, X. L.; Shen, P. C.; Tang, B. Z.; Zhao, Z. J. Efficient circularly polarized electroluminescence from achiral luminescent materials. *Angew. Chem., Int. Ed.* **2023**, *62*, e202300492.

[33] Dong, Q. W.; Xiao, C.; He, B. H.; Yang, X. F.; Zeng, S. K.; Zhong, Q. H.; Duan, P. F.; Zhu, W. G.; Wang, Y. F. Binaphthol-based chiral host molecules for efficient solution-processed circularly polarized OLEDs. *Chem. Commun.* **2023**, *59*, 1473–1476.

[34] Dong, Q. W.; He, B. H.; Qiao, W. J.; Zhu, W. G.; Duan, P. F.; Wang, Y. F. A chiral bipolar host for efficient solution-processed circularly polarized OLEDs via a chirality energy transfer process. *Chem. Commun.* **2024**, *60*, 3421–3424.

[35] Geng, Z. X.; Zhang, Y. X.; Zhang, Y.; Li, Y.; Quan, Y. W.; Cheng, Y. X. Circularly polarized electroluminescence from an achiral fluorophore induced by co-assembly with chiral polymers. *J. Mater. Chem. C* **2021**, *9*, 12141–12147.

[36] Geng, Z. X.; Zhang, Y. X.; Zhang, Y.; Quan, Y. W.; Cheng, Y. X. Amplified circularly polarized electroluminescence behavior triggered by helical nanofibers from chiral co-assembly polymers. *Angew. Chem.* **2022**, *134*, e202202718.

[37] Geng, Z. X.; Liu, Z.; Li, H.; Zhang, Y.; Zheng, W. H.; Quan, Y. W.; Cheng, Y. X. Inverted and amplified CP-EL behavior promoted by AIE-active chiral co-assembled helical nanofibers. *Adv. Mater.* **2023**, *35*, 2209495.

[38] Zhang, Y.; Li, D.; Li, Q. H.; Quan, Y. W.; Cheng, Y. X. High comprehensive circularly polarized electroluminescence performance improved by chiral coassembled host materials. *Adv. Funct. Mater.* **2023**, *33*, 2309133.

[39] Guo, C. H.; Zhang, Y. W.; Zhao, W. L.; Tan, K. K.; Feng, L. H.; Duan, L.; Chen, C. F.; Li, M. Chiral co-assembly with narrowband multi-resonance characteristics for high-performance circularly polarized organic light-emitting diodes. *Adv. Mater.* **2024**, *36*, 2406550.

[40] Chen, Z. X.; Zhong, C.; Han, J. M.; Miao, J. S.; Qi, Y. Y.; Zou, Y.; Xie, G. H.; Gong, S. L.; Yang, C. L. High-performance circularly polarized electroluminescence with simultaneous narrowband emission, high efficiency, and large dissymmetry factor. *Adv. Mater.* **2022**, *34*, 2109147.

[41] Gu, Q.; Chen, Z. J.; Xie, W. T.; Qiu, W. D.; Peng, X. M.; Jiao, Y. H.; Li, M. K.; Liu, Z.; Sun, G. W.; Lu, Y. F. et al. Chiral exciplex acceptor enables circularly polarized electroluminescence with high dissymmetry factor close to 10^{-2}. *Adv. Opt. Mater.* **2022**, *10*, 2201793.
[42] Chen, Z. X.; Huang, M. L.; Zhong, C.; Cao, X. S.; Xie, G. H.; Gong, S. L.; Yang, C. L. Cascade chirality transfer through diastereomeric interaction enables efficient circularly polarized electroluminescence. *Adv. Funct. Mater.* **2023**, *33*, 2215179.
[43] Zhong, X. S.; Yuan, L.; Liao, X. J.; Hu, J. J.; Xing, S.; Song, S. Q.; Xi, J. Q.; Zheng, Y. X. Circularly polarized organic light-emitting diodes based on chiral hole transport enantiomers. *Adv. Mater.* **2024**, *36*, 2311857.
[44] Huo, P. H.; Yang, T. Y.; Fang, P. Y.; Li, Y. J.; Zheng, N. L.; Gong, M.; Bian, Z. Q.; Liu, Z. W. Chiral electron transporting material for circularly polarized organic light-emitting diode. *Sci. China Chem.* **2024**, *67*, 3777–3784.
[45] Wu, Z. G.; Han, H. B.; Yan, Z. P.; Luo, X. F.; Wang, Y.; Zheng, Y. X.; Zuo, J. L.; Pan, Y. Chiral octahydro-binaphthol compound-based thermally activated delayed fluorescence materials for circularly polarized electroluminescence with superior EQE of 32.6% and extremely low efficiency roll-off. *Adv. Mater.* **2019**, *31*, 1900524.
[46] Ai, L.; Wang, H. L.; Wang, B. Y.; Liu, S. Y.; Song, H. Q.; Lu, S. Y. Concentration-switchable assembly of carbon dots for circularly polarized luminescent amplification in chiral logic gates and deep-red light-emitting diodes. *Adv. Mater.* **2024**, *36*, 2410094.
[47] Yan, Z. P.; Liu, T. T.; Wu, R. X.; Liang, X.; Li, Z. Q.; Zhou, L.; Zheng, Y. X.; Zuo, J. L. Chiral thermally activated delayed fluorescence materials based on *R/S*-*N*2,*N*2'-diphenyl-[1,1'-binaphthalene]-2,2'-diamine donor with narrow emission spectra for highly efficient circularly polarized electroluminescence. *Adv. Funct. Mater.* **2021**, *31*, 2103875.
[48] Rhee, S.; Jung, D.; Kim, D.; Lee, D. C.; Lee, C.; Roh, J. Polarized electroluminescence emission in high-performance quantum rod light-emitting diodes via the Langmuir-Blodgett technique. *Small* **2021**, *17*, 2101204.
[49] Duan, T. W.; Ai, J.; Chen, S. J.; He, G. F.; Guo, X. J.; Han, L.; Che, S. N.; Duan, Y. Y. Chiral CdSe/CdS quantum dot (in rod)-light-emitting diodes with circularly polarized electroluminescence. *Nano Res.* **2022**, *15*, 9573–9577.
[50] Hikmet, R. A. M.; Chin, P. T. K.; Talapin, D. V.; Weller, H. Polarized-light-emitting quantum-rod diodes. *Adv. Mater.* **2005**, *17*, 1436–1439.
[51] Rizzo, A.; Nobile, C.; Mazzeo, M.; De Giorgi, M.; Fiore, A.; Carbone, L.; Cingolani, R.; Manna, L.; Gigli, G. Polarized light emitting diode by long-range nanorod self-assembling on a water surface. *ACS Nano* **2009**, *3*, 1506–1512.
[52] Wei, Y. P.; Xu, Y. Y.; Wang, Q.; Wang, J. Y.; Lu, H. B.; Zhu, J. $CsPbBr_3$ nanowire polarized light-emitting diodes through mechanical rubbing. *Chem. Commun.* **2020**, *56*, 5413–5416.
[53] Song, Y.; Liu, R. X.; Wang, Z. B.; Xu, H. Y.; Ma, Y.; Fan, F. J.; Voznyy, O.; Du, J. F. Enhanced emission directivity from asymmetrically strained colloidal quantum dots. *Sci. Adv.* **2022**, *8*, eabl8219.
[54] Jang, G.; Jo, D. Y.; Ma, S.; Lee, J.; Son, J.; Lee, C. U. Jeong, W; Yang, S.; Park, J. H.; Yang, H. et al. Core–shell perovskite quantum dots for highly selective room-temperature spin light-emitting diodes. *Adv. Mater.* **2024**, *36*, 2309335.
[55] Wang, Q. Q.; Zhu, H. M.; Tan, Y. Z.; Hao, J. J.; Ye, T. K.; Tang, H. D.; Wang, Z. J.; Ma, J. R.; Sun, J. Y.; Zhang, T. Q. et al. Spin quantum dot light-emitting diodes enabled by 2D chiral perovskite with spin-dependent carrier transport. *Adv. Mater.* **2024**, *36*, 2305604.
[56] Mustaqeem, M.; Chou, P. T.; Kamal, S.; Ahmad, N.; Lin, J. Y.; Lu, Y. J.; Lee, X. H.; Lin, K. H.; Lu, K. L.; Chen, Y. F. Solution-processed and room-temperature spin light-emitting diode based on quantum dots/chiral metal-organic framework heterostructure. *Adv. Funct. Mater.* **2023**, *33*, 2213587.
[57] Kim, Y. H.; Zhai, Y. X.; Lu, H. P.; Pan, X.; Xiao, C. X.; Gaulding, E. A.; Harvey, S. P.; Berry, J. J.; Vardeny, Z. V.; Luther, J. M. et al. Chiral-induced spin selectivity enables a room-temperature spin light-emitting diode. *Science* **2021**, *371*, 1129–1133.
[58] He, S.; Lin, W. X.; Yu, D.; Shi, J. W.; Yin, Z.; Sun, C. J.; Liu, H. L.; Zhang, C.; Yuan, J. Y.; Bai, S. et al. Perovskite spin light-emitting diodes with simultaneously high electroluminescence dissymmetry and high external quantum efficiency. *Nat. Commun.* **2025**, *16*, 2201.
[59] Ye, C. Y.; Jiang, J. W.; Zou, S. L.; Mi, W. B.; Xiao, Y. Core–shell three-dimensional perovskite nanocrystals with chiral-induced spin selectivity for room-temperature spin light-emitting diodes. *J. Am. Chem. Soc.* **2022**, *144*, 9707–9714.
[60] Feng, L. Z.; Song, Y. H.; Li, Z. D.; Zhu, B. S.; Ma, Z. Y.; Yang, J. N.; Yin, Y. C.; Hao, J. M.; Ding, G. J.; Wang, Y. R. et al. Dimensional and doping engineering of chiral perovskites with enhanced spin selectivity for green emissive spin light-emitting diodes. *Nano Lett.* **2024**, *24*, 6084–6091.
[61] Gao, H. T.; Chen, Y.; Zhang, R. X.; Cao, R.; Wang, Y.; Tian, Y. F.; Xiao, Y. Dual-ligand quasi-2D perovskites with chiral-induced spin selectivity for room temperature spin-LEDs. *Mater. Horiz.* **2024**, *11*, 2906–2913.
[62] Yao, J. W.; Wang, Z. Y.; Huang, Y. L.; Xue, J.; Zhang, D. L.; Chen, J. S.; Chen, X. H.; Dong, S. C.; Lu, H. P. Efficient green spin light-emitting diodes enabled by ultrafast energy- and spin-funneling in chiral perovskites. *J. Am. Chem. Soc.* **2024**, *146*, 14157–14165.
[63] Zhang, R. X.; Tian, Y. F.; Ye, C. Y.; Wang, Y.; Mi, W. B.; Dai, H. T.; Zou, S. L.; Cao, R.; Gao, H. T.; Xiao, Y. Efficient quasi-2D perovskite spin light-emitting diodes based on chiral-induced spin selectivity. *Chem. Mater.* **2024**, *36*, 3812–3819.
[64] Yang, C. H.; Xiao, H.; Sang, Y. F.; Luo, J.; Xiao, S. B.; Xuan, H. L.; Ding, Q. R.; Lin, W. L.; Xu, Z. X.; Chen, Z. N. et al. *In situ* formed perovskite nanocrystal films toward efficient circularly polarized electroluminescence. *Adv. Funct. Mater.* **2024**, *34*, 2310500.
[65] Li, B. H.; Li, Y.; Yuan, W.; Zhang, X. P.; Tao, S.; Zhan, H. M.; Yu, Z. G.; Wang, K.; Liu, J.; Wang, L. X. et al. Chiral quasi-2D perovskites based single junction spin-light-emitting diodes. *Adv. Funct. Mater.* **2025**, *35*, 2415433.
[66] Cho, C.; Greenham, N. C. Computational study of dipole radiation in re-absorbing perovskite semiconductors for optoelectronics. *Adv. Sci.* **2021**, *8*, 2003559.
[67] Xia, Y. J.; Li, H. B.; Vaskeviciute, M.; Faccio, D.; Karimullah, A. S.; Heidari, H.; Ghannam, R. Temperature-tunable cholesteric liquid crystal optical combiners for extended reality applications. *Adv. Intell. Syst.* **2025**, *7*, 2400411.
[68] St. John, W. D.; Fritz, W. J.; Lu, Z. J.; Yang, D. K. Bragg reflection from cholesteric liquid crystals. *Phys. Rev. E* **1995**, *51*, 1191–1198.
[69] Goodby, J. W.; Collings, P. J.; Kato, T.; Tscierske, C.; Gleeson, H. F.; Raynes, P. *Handbook of Liquid Crystals*; John Wiley & Sons: Hoboken, 2014.
[70] Holl, H. B. Specular reflection and characteristics of reflected light. *J. Opt. Soc. Am.* **1967**, *57*, 683–690.
[71] Xia, Y. J.; Ahmed, Z.; Karimullah, A.; Mottram, N.; Heidari, H.; Ghannam, R. Thermal-controlled cholesteric liquid crystal wavelength filter lens for photosensitive epilepsy treatment. *Cell Rep. Phys. Sci.* **2024**, *5*, 102158.
[72] Guo, Q.; Li, Z. Y.; Zhou, Y. J.; Zhao, S. S.; Wang, Y. X.; Zhang, M. J.; Li, G. G.; Tong, Z.; Zhuang, T. T.; Yu, S. H. Self-positioning microdevices enable adaptable spatial displaying. *Sci. Adv.* **2025**, *11*, eadv2721.